Journal of Physics: Condensed Matter

PAPER

Incorporation of Ti in epitaxial Fe_2TiO_4 thin films

To cite this article: Tiffany C Kaspar *et al* 2021 *J. Phys.: Condens. Matter* **33** 314004

IOP Publishing Journal of Physics: Condensed Matter
J. Phys.: Condens. Matter **33** (2021) 314004 (10pp) https://doi.org/10.1088/1361-648X/ac0571

Incorporation of Ti in epitaxial Fe_2TiO_4 thin films

Tiffany C Kaspar[1,*], Steven R Spurgeon[2], Bethany E Matthews[2], Mark E Bowden[3], Steve M Heald[4], Le Wang[1], Ron Kelley[5], Rajendra Paudel[6], Tamara Isaacs-Smith[6], Ryan B Comes[6], Xinmao Yin[7,8], Chi Sin Tang[7,8], Andrew T S Wee[8] and Scott A Chambers[1]

[1] Physical and Computational Sciences Directorate, Pacific Northwest National Laboratory, Richland, WA, United States of America
[2] Energy and Environment Directorate, Pacific Northwest National Laboratory, Richland, WA, United States of America
[3] Environmental Molecular Sciences Laboratory, Pacific Northwest National Laboratory, Richland, WA, United States of America
[4] Advanced Photon Source, Argonne National Laboratory, Argonne, IL, United States of America
[5] ThermoFisher Scientific, Hillsboro, OR, United States of America
[6] Department of Physics, Auburn University, Auburn, AL, United States of America
[7] Singapore Synchrotron Light Source, National University of Singapore, Singapore
[8] Department of Physics, Faculty of Science, National University of Singapore, Singapore

E-mail: tiffany.kaspar@pnnl.gov

Received 25 March 2021, revised 28 April 2021
Accepted for publication 26 May 2021
Published 17 June 2021

Abstract

The titanomagnetites ($Fe_{2-x}Ti_xO_4$, $x \leqslant 1$) are a family of reducible spinel-structure oxides of interest for their favorable magnetic, catalytic, and electrical transport properties. To understand the stability of the system during low temperature deposition, epitaxial thin films of Fe_2TiO_4 were deposited by molecular beam epitaxy (MBE) on MgO(001) at 250–375 °C. The homogeneous incorporation of Ti, Fe valence state, and film morphology were all found to be strongly dependent on the oxidation conditions at the low substrate temperatures employed. More oxidizing conditions led to phase separation into epitaxial, faceted Fe_3O_4 and rutile TiO_2. Less oxidizing conditions resulted in polycrystalline films that exhibited Ti segregation to the film surface, as well as mixed Fe valence (Fe^{3+}, Fe^{2+}, Fe^0). A narrow window of intermediate oxygen partial pressure during deposition yielded nearly homogeneous Ti incorporation and a large fraction of Fe^{2+}. However, these films were poorly crystallized, and no occupation of tetrahedral sites in the spinel lattice by Fe^{2+} was detected by x-ray magnetic circular dichroism at the Fe L-edge. After vacuum annealing, a small fraction of Fe^{2+} was found to occupy tetrahedral sites. Comparison of these results with previous work suggests that the low temperature deposition conditions imposed by use of MgO substrates limits the incorporation of Ti into the spinel lattice. This work suggests a path towards obtaining stoichiometric, well-crystallized Fe_2TiO_4 by MBE by utilizing high substrate temperature and low oxygen partial pressure during deposition on thermally stable substrates.

Keywords: magnetite, ulvospinel, titanomagnetite, molecular beam epitaxy

Supplementary material for this article is available online

(Some figures may appear in colour only in the online journal)

*Author to whom any correspondence should be addressed.

1. Introduction

The iron oxides comprise a classical family of reducible oxides. The favorable catalytic and magnetic properties of iron oxides, including magnetite and the spinel ferrites, are well established [1–5], and many of these properties are intimately tied to the reducible nature of the Fe valence. Titanomagnetites, $Fe_{3-x}Ti_xO_4$, are a well-known family of reducible iron oxides because they are the most abundant magnetic ores of igneous rocks, making them of geophysical and petrological interest [6–8]. More recently, $Fe_{3-x}Ti_xO_4$ has been explored as a stable source of Fe^{2+} for heterogeneous catalysis [9–12]. Fe valence change across the titanomagnetite composition range also leads to unique electronic properties. For Ti^{4+} fractions of $x < \sim 0.6$, titanomagnetite exhibits *n*-type semiconducting transport properties, but for $x \geqslant \sim 0.6$ and including ulvöspinel, Fe_2TiO_4, the material exhibits *p*-type conductivity [8]. $Fe_{3-x}Ti_xO_4$ is thus one of only a few known *p*-type iron oxide spinels [13, 14].

Magnetite, Fe_3O_4, has the inverse spinel structure, AB_2O_4, with the tetragonal sites occupied (nearly) exclusively by Fe^{3+}, and the octahedral sites occupied by equal fractions of Fe^{2+} and Fe^{3+} [15, 16]. Magnetite exhibits metallic conductivity via electron hopping between Fe^{2+} and Fe^{3+} on octahedral sites [17]. In the titanomagnetite series, substitutional Ti^{4+} replaces Fe^{3+} on the octahedral sites, and an equal fraction of remaining Fe^{3+} is reduced to Fe^{2+} to maintain charge neutrality [6–8, 18, 19]. The Fe^{2+}/Fe^{3+} site occupancy at $x < 1$ remains controversial, but is likely in part a function of the lattice strain induced by doping smaller Ti^{4+} into the lattice [7, 8, 18, 19]. At temperatures <550 °C, titanomagnetites exhibit a miscibility gap, separating (at thermodynamic equilibrium) into Fe_3O_4 and Fe_2TiO_4 [20].

The synthesis of titanomagnetites is made challenging by the complex interplay between temperature and oxygen activity on phase stability [21, 22]; only in a narrow window of parameter space is stoichiometric $Fe_{3-x}Ti_xO_4$ obtained [19, 23]. There are a few reports of the successful growth of epitaxial thin films of $Fe_{3-x}Ti_xO_4$ by pulsed laser deposition (PLD) [23–25]. Murase *et al*. [24] deposited $Fe_{2.4}Ti_{0.6}O_4(111)$ films on $Al_2O_3(0001)$ substrates and obtained single-phase spinel, as determined by x-ray diffraction (XRD), under low-oxygen deposition conditions (7.5×10^{-8} Torr O_2). The valence states and site occupancies of the cations were not determined. Yamahara *et al* [25] deposited $Fe_{3-x}Ti_xO_4(001)$ films ($0 \leqslant x \leqslant 0.8$) on $MgAl_2O_4(001)$ substrates, and obtained single-phase films under low-oxygen deposition conditions similar to those employed by Murase *et al* [24]. *Ex situ* x-ray absorption spectroscopy (XAS) measurements at the Fe L-edge of films capped with a thin layer of Al_2O_3 to prevent surface oxidation revealed an increasing contribution of Fe^{2+} as the Ti concentration increased. Fitting the Fe^{2+} and Fe^{3+} contributions at the Fe L-edge produced average Fe valences that were consistent with those expected from the nominal stoichiometry of each film. Droubay *et al* [23] deposited single-phase $Fe_{3-x}Ti_xO_4$ films ($0 \leqslant x \leqslant 1$) on MgO(001) without the intentional introduction of O_2 into the deposition chamber (partial pressure of $O_2 < 10^{-8}$ Torr). *Ex situ* measurement of Fe valence by x-ray photoelectron spectroscopy (XPS) and x-ray absorption near edge spectroscopy (XANES) showed that the Fe^{2+}/Fe^{3+} ratio systematically increased with increasing Ti concentration, but the formal valence of Fe near the film surface was closer to Fe^{3+} than expected from the composition. This was confirmed by x-ray magnetic circular dichroism (XMCD) measurements at the Fe L-edge, collected in the surface-sensitive total electron yield (TEY) mode, which produced a smaller tetrahedral Fe^{2+} contribution than predicted. It was hypothesized that the surface region was comprised of a titanomaghemite-like layer that was enriched in Ti relative to the film bulk. Ti enrichment of the film surface was confirmed in later studies [26, 27].

In this paper, we revisit the deposition of $Fe_{3-x}Ti_xO_4$ films. Drawing on previous reports of the deposition of Fe_3O_4 [28–30] and Fe_2CrO_4 [31–33], $Fe_{3-x}Ti_xO_4$ films are deposited with molecular beam epitaxy (MBE) to achieve a higher level of control over oxygen stoichiometry in the films than typically afforded by PLD. Advanced multimodal characterization is employed to establish correlations between the oxygen pressure during deposition and both the Fe valence and the extent of spatial segregation of Ti. Our results offer insight into the energetics of the $Fe_{3-x}Ti_xO_4$ system, and suggest pathways to achieve high quality thin films of $Fe_{3-x}Ti_xO_4$ for subsequent study of electronic, magnetic, or catalytic properties.

2. Experimental methods

Thin films of $Fe_{3-x}Ti_xO_4$ were deposited by MBE on single crystal MgO(001) substrates. The MgO substrates were prepared by first etching in 85% H_3PO_4 for 45 s to remove surface oxyhydroxides, then annealing in pairs with the epi-polished surfaces in contact for 4 h at 1125 °C in air, as described previously [34]. After cooldown, the substrates were immediately mounted and transferred to an ultraviolet/ozone cleaner for 5 min, then loaded into the ultrahigh vacuum (UHV) system. Substrates were cleaned *in situ* by exposing to activated oxygen at a chamber pressure of 3×10^{-6} Torr from an electron cyclotron resonance (ECR) microwave plasma source at room temperature for 30 min, and this flow was maintained as the substrate was heated to the desired deposition temperature (250–375 °C). Depending on the desired oxidation regime, depositions either occurred in this same oxygen flow or with the plasma switched off and a decreased oxygen flow. Fe and Ti were evaporated from high temperature effusion cells; the $Fe_{3-x}TiO_4$ growth rate was maintained at 0.085 Å s^{-1} for all Ti doping levels. Final film thicknesses were 30–50 nm. All samples were rotated at 1 rpm during the growth, except for the film deposited at condition A, which was stationary. Surface crystallinity and morphology of both the substrates before growth and the films during and after deposition were monitored by *in situ* reflection high energy electron diffraction (RHEED).

After cooling in vacuum, films were transferred under UHV to an appended chamber for *in situ* x-ray photoelectron spectroscopy (XPS) using a VG/Scienta R3000 analyzer with monochromatic Al K_α x-rays. A low energy electron flood gun was used to neutralize surface charging. All spectra were shifted to align the O 1*s* peak to 531.35 eV, which was found to

be the absolute binding energy (BE) position of the O 1*s* core level peak measured on epitaxial Fe_3O_4 and Fe_2CrO_4 films that were sufficiently semiconducting to allow XPS measurements without the use of the flood gun for charge compensation [31].

Ex situ high-resolution XRD patterns were collected using a Rigaku SmartLab diffractometer with a rotating Cu anode operated at 45 kV and 200 mA. The incident beam (Cu K_α) was filtered using a two-bounce Ge(220) monochromator, and a matching monochromator was employed for the diffracted beam. Rutherford backscattering spectrometry (RBS) measurements were conducted at Auburn University using a 6HDS-2 tandem National Electrostatics Corporation Pelletron with 2 sources for ions, an alphatross (rf source for production of He^+) and SNICS source (source of negative ions by cesium sputtering). Measurements were made using a He^{2+} ion beam energy of 1.972 MeV, an incident angle $\alpha = 0°$, an exit angle $\beta = 10°$, and a scattering angle $\theta = 170°$. Fits to the experimental data were completed using the analysis software SIMNRA (simnra.com).

Cross-sectional scanning transmission electron microscopy (STEM) samples were prepared using FEI Helios NanoLab Ga^+ Focused Ion Beam (FIB) and Thermo Fisher Helios G4 UXe Plasma Focused Ion Beam (PFIB) DualBeam microscopes with a standard lift out procedure. STEM high-angle annular dark field (STEM-HAADF) images were collected on a probe-corrected JEOL GrandARM-300F microscope operating at 300 kV, with a convergence semi-angle of 29.7 mrad and a collection angle range of 75–515 mrad. To improve signal-to-noise ratio and remove scan artifacts, drift-corrected images were prepared using the SmartAlign plugin [35]; for this, a series of ten frames were collected at 1024 × 1024 pixels with a 2 μs px^{-1} dwell time and 90° rotations between frames. A rigid alignment was performed, followed by non-rigid alignment. Portions of the image in figure 4 were then processed using template matching to further enhance signal-to-noise. Electron energy loss spectroscopy (STEM-EELS) was performed with a 0.25 eV ch^{-1} dispersion, yielding an effective ∼0.75 eV energy resolution. Data was collected in the DualEELS mode to correct for energy drift.

XANES at the Fe K-edge was collected on the PNC/XSD beamline 20-BM at the Advanced Photon Source at Argonne National Laboratory. Measurements were made in fluorescence mode with the x-ray polarization perpendicular to the surface and the incident beam at a glancing angle of ∼5° off the surface. All samples were continuously rotated about the surface normal during the measurement. A Si(111) double crystal monochromator was used, resulting in an energy resolution (ΔE) defined by $\Delta E/E = 1.4 \times 10^{-4}$, where E is the x-ray energy.

Fe L-edge XMCD patterns were collected at the Surface, Interface and Nanostructure Science (SINS) beamline at the Singapore Synchrotron Light Source, National University of Singapore using the total electron yield (TEY) detection method. The XMCD signal is the difference between absorption spectra obtained with $a + 1$T and $a - 1$T magnetic field, set parallel to the x-ray beam direction, using plus helicities of circular polarized light. The grazing-incident spectra were measured at $\theta = 60°$.

3. Results

3.1. Cation valence

Fe_2TiO_4 films were deposited by oxygen-assisted molecular beam epitaxy (OA-MBE) at various oxygen pressures to evaluate the effect of oxidizing conditions on the resulting oxidation state of the film. Figure 1(a) shows Fe 2*p* core level XPS spectra for five Fe_2TiO_4 films deposited under the conditions outlined in table 1. The Fe $2p_{3/2}$ manifold is complex [31, 36–38], so we limit our discussion of the data in figure 1(a) to a qualitative comparison of the lineshape to that for magnetite (Fe^{2+}:Fe^{3+} = 0.33:0.67) and hematite (Fe^{3+}). A clear trend is observed as the oxidizing environment during deposition is lessened from condition B to condition C, then to condition E. The lineshape of the Fe 2*p* peak from Fe_2TiO_4 deposited at condition B exhibits a well-defined shoulder (∼709 eV) on the low binding energy side of the Fe $2p_{3/2}$ peak, which is attributed to Fe^{2+}; the main peak at ∼711 eV is attributed to Fe^{3+} [1, 16]. In the absence of cation vacancies, Fe_2TiO_4 will contain exclusively Fe^{2+}. However, an inspection of the Fe 2*p* lineshape for the Fe_2TiO_4 film deposited under condition B reveals a significant contribution of Fe^{3+}. The Fe^{2+} shoulder, relative to the Fe^{3+} peak, is not as large as that in Fe_3O_4. Slight intensity at ∼719 eV is likely due to the presence of a weak Fe^{3+} satellite [28]. Using the measured stoichiometry of this film obtained from fits to RBS data (supplementary material figure S1) (https://stacks.iop.org/JPCM/33/314004/mmedia), $x = 0.86$, the expected Fe^{2+} fraction is ∼0.87, which is still a significantly larger Fe^{2+} content than that for Fe_3O_4. Deposition in the less oxidizing environment of condition C increases the Fe^{2+} shoulder relative to the Fe^{3+} peak, as expected. Note, however, that the increase is slight and a significant Fe^{3+} contribution is still present. Reducing the oxygen partial pressure even further, to conditions D and E, leads to dramatic changes in the Fe 2*p* manifold: a strong peak appears at ∼707 eV, revealing the presence of a significant concentration of metallic Fe^0. Interestingly, however, despite the reduced nature of the film indicated by Fe^0, the broadened peak at ∼710–711 eV shows that, for the film under condition D, the oxidized Fe is still dominated by Fe^{3+}, and even under condition E, the Fe^{2+} contribution has nearly equaled, but not surpassed, that of Fe^{3+}. A weak Fe^{2+} satellite at ∼714–716 eV [28] is observed, but the presence of the nearby Fe^{3+} satellite peak is partially obscured by the Fe $2p_{1/2}$ peak of Fe^0.

The Fe^{2+} fraction of the Fe_2TiO_4 film deposited under condition C was successfully increased by annealing the film in vacuum at 400 °C for 2 h. Under these conditions, the relative fraction of Fe^{2+} measured by XPS increased significantly relative to the Fe^{3+} fraction, as shown in figure 1(a). There is no evidence of Fe^0, but a small fraction of Fe^{3+} is still present.

To assess whether the surface-sensitive Fe 2*p* XPS data is representative of the bulk of the Fe_2TiO_4 film, Fe K-edge XANES spectra were collected in the bulk-sensitive fluorescence yield (FY) mode for films deposited at conditions B and C. These spectra are presented in figure 1(b), along with reference spectra of FeO, Fe_3O_4, and Fe_2O_3. Qualitatively, the

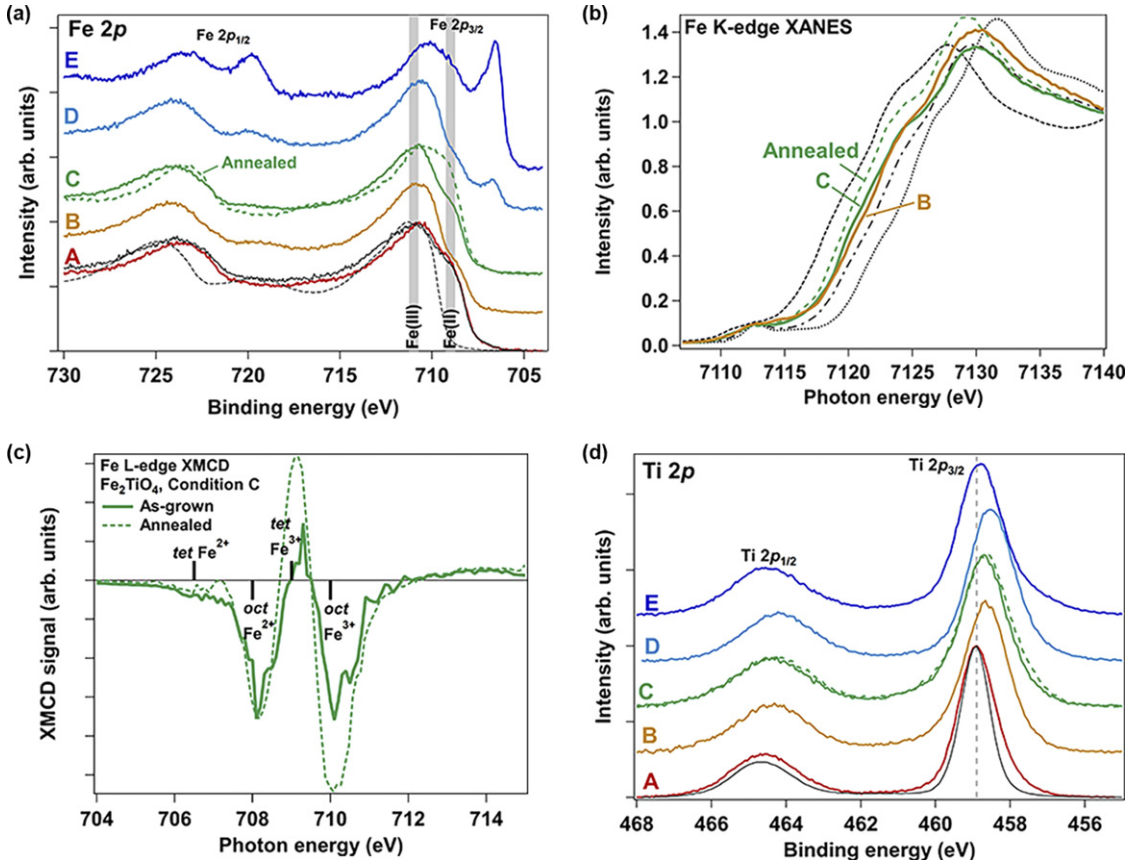

Figure 1. Spectroscopy of Fe_2TiO_4 films deposited under various conditions. (a) Fe 2*p* core level XPS spectra. Spectra are normalized to the Fe^{3+} $2p_{3/2}$ peak near 711 eV, and offset vertically for clarity. Reference spectra for epitaxial thin films of Fe_2O_3 (thin dashed) and Fe_3O_4 (thin solid) are also plotted. Approximate positions of Fe^{3+} and Fe^{2+} are denoted with gray bars. (b) FY mode Fe K-edge XANES spectra of films deposited under conditions B, C, and C after vacuum annealing. Spectra are normalized to the edge jump height. Also plotted are reference standards for Fe_2O_3 (dotted), Fe_3O_4 (dash-dot), and FeO (dashed). (c) Fe L-edge XMCD signal for film deposited under condition C before and after vacuum annealing. Reference peak/valley positions [19] are also indicated. (d) Ti 2*p* core level XP spectra. Spectra are normalized to the Ti^{4+} $2p_{3/2}$ peak near 459 eV. Reference Ti 2*p* spectrum from rutile TiO_2 single crystal is also plotted (thin solid), and its position (458.9 eV) is indicated (dashed).

Table 1. Conditions for deposition of Fe_2TiO_4 by OA-MBE.

Condition	O_2 pressure (Torr)	Oxygen plasma?	Substrate temperature
A	3×10^{-6}	Yes	375 °C
B	1×10^{-6}	No	250 °C
C	4×10^{-7}	No	250 °C
C_{anneal}	$<2 \times 10^{-8}$	—	400 °C/120 min
D	3×10^{-7}	No	300 °C
E	2×10^{-7}	No	250 °C

leading absorption edge of the film at condition B falls between those for Fe_3O_4 and FeO, indicating that the Fe_2TiO_4 film possesses more Fe^{2+} than does magnetite. This is in contrast to the Fe 2*p* core level XPS data in figure 1(a), which indicated that less Fe^{2+} was present than in magnetite. The Fe_2TiO_4 film deposited at condition C shows a leading edge that is closer to FeO, and this edge shifts nearer to that of FeO after annealing. An approximate quantification of the fractions of Fe^{2+} and Fe^{3+} present in these films can be made by assuming that the leading edge position (taken at half the normalized edge jump height) shifts linearly with the addition of Fe^{2+} from the position for Fe_2O_3 to the position for FeO. From this analysis, the Fe^{2+} fraction of the film at condition B is ∼0.45, while the Fe^{2+} fraction of the film at condition C is ∼0.60, and after annealing this fraction increases further to ∼0.66. Note that this increase in Fe^{2+} fraction with annealing is less than that qualitatively predicted from comparing the XPS data of the film before and after annealing. This discrepancy between the surface-sensitive, *in situ* XPS and whole-film sensitive, *ex situ* XANES data suggests that the as-grown film surface is more oxidized than the underlying bulk, whereas vacuum annealing preferentially reduces the film surface, as indicated

by the significant increase in Fe^{2+} measured by *in situ* XPS after annealing. The lower Fe^{2+} fraction measured by *ex situ* XANES arises because the bulk of the film has not reduced as effectively, and in addition, a portion of the reduced surface may re-oxidize to Fe^{3+} upon air exposure.

Site occupancy of Fe^{2+} and Fe^{3+} in the spinel lattice can be determined from the Fe L-edge XMCD signal in figure 1(c) for the film deposited at condition C as-grown and after annealing. As detailed previously [19], the structure of the Fe Le-dge XMCD signal arises from occupancy of tetrahedral (*tet*, positive peaks) and octahedral (*oct*, negative peaks) sites in the spinel lattice by Fe^{2+} (lower energy) and Fe^{3+} (higher energy). As shown in figure 1(c), both before and after annealing, Fe^{3+} is present in both tetrahedral and octahedral sites. After annealing, the XMCD signal in both sites increases due to the improved crystalline order of the film. Because of this overall increase in XMCD signal, it is difficult to evaluate whether the Fe^{3+}_{tet} occupancy decreases after annealing due to an increased concentration of Fe^{2+} on these sites. However, an inspection of the Fe^{2+}_{tet} signal shows a complete lack of Fe^{2+}_{tet} occupancy in the as-grown film. After annealing, a small positive signal appears, indicating the presence of a small fraction of Fe^{2+}_{tet}. However, a much larger signal is expected for full Fe^{2+}_{tet} occupancy in stoichiometric Fe_2TiO_4 [19].

The trend shown in figures 1(a) and (b) of reduced cation valence with more reducing deposition conditions is also observed for the Ti 2*p* XPS core level spectra in figure 1(d), although the Ti valence changes are much more subtle than those of Fe. Fe_2TiO_4 films deposited at conditions B and C both contain Ti^{4+}, as expected [19]. There is no clear evidence of a tail at lower BE due to Ti^{3+}, but the Ti $2p_{3/2}$ peak is considerably broadened (Ti $2p_{3/2}$ spectrum from condition C: FWHM = 1.47 eV) and shifted to lower BE (δBE ~ -0.2 eV) compared to the sharp Ti^{4+} peak typically observed (rutile TiO_2 reference spectrum: BE = 458.9 eV, FWHM = 0.91 eV). After annealing in vacuum, the Ti $2p_{3/2}$ peak broadens further (FWHM = 1.58 eV), but remains symmetric. In the most reducing deposition environment used, condition E, the Ti $2p_{3/2}$ peak exhibits slightly increased intensity at lower BE, indicating the presence of a small fraction of Ti^{3+}. Peak fitting indicates that the Ti^{3+} contribution is less than 5% of the total Ti $2p_{3/2}$ peak area. The BE shift of the Ti^{4+} peak relative to the Ti $2p_{3/2}$ spectrum from $SrTiO_3$ is ~0.1 eV, less than the shifts of spectra from conditions B, C, and D.

The Fe_2TiO_4 film deposited in the more oxidizing environment at condition A presents an anomaly to the Fe 2*p* and Ti 2*p* spectral trends discussed above. Despite the oxidizing conditions, the Fe $2p_{3/2}$ lineshape indicates an Fe^{2+} fraction similar to that of magnetite (0.33). This is a larger fraction of Fe^{2+} than that observed in the Fe 2*p* spectrum for the film deposited at condition B, despite the more strongly oxidizing environment of condition A.

The Ti 2*p* XPS spectrum from the film at condition A also shows differences compared to the spectra at conditions B and C: the Ti 2*p* lineshape is significantly narrower (FWHM = 1.15 eV), and the peak position is well aligned with the reference Ti 2*p* spectrum from $SrTiO_3$. Comparing

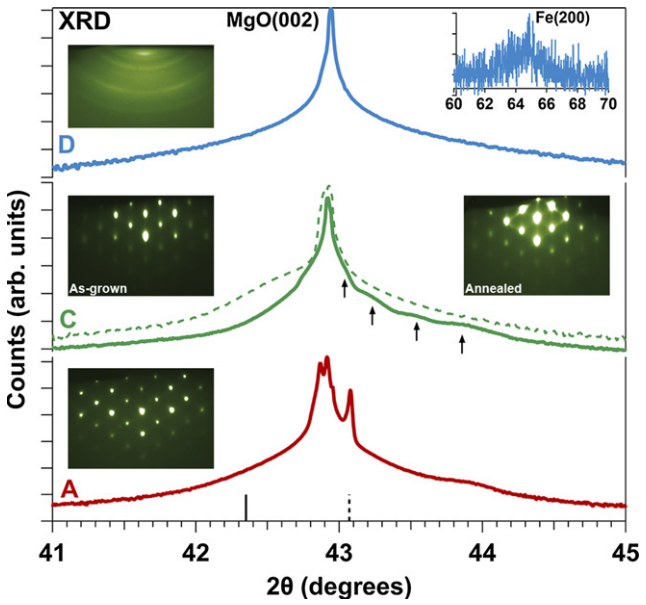

Figure 2. XRD θ–2θ and RHEED [110] azimuth patterns of Fe_2TiO_4 films deposited under conditions A, C, C after annealing (dashed), and D. Positions of bulk Fe_2TiO_4(004) (solid stick) and Fe_3O_4(004) (dashed stick) reflections are indicated. Inset: Fe(200) reflection from film deposited under condition D.

the Ti 2*p* and Fe 2*p* peak areas using tabulated photoemission cross-sections [39] results in a measured Ti concentration of $x = 1.62$, which is significantly enhanced compared to the target stoichiometry of $x = 1$. In contrast, the same analysis of the film at condition B reveals $x = 1.08$, and $x = 1.01$ for the film at condition C (compare to the RBS measurement of $x = 0.86$). The films deposited at conditions D and E also exhibited values of x significantly higher than the expected stoichiometry ($x = 1.93$ at condition D and $x = 2.13$ at condition E).

As shown in supplementary material figure S2, deposition at 375 °C has resulted in a small amount of Mg segregation to the film surface. This segregation is not observed for films deposited at 250–300 °C. However, annealing the film deposited at condition C at 400 °C results in some surface segregation of Mg.

3.2. Film structure and cation distribution

Neither the Fe_2TiO_4 film deposited at condition A nor the film deposited at condition C exhibited a reflection at the expected d-spacing for Fe_2TiO_4(001) in θ–2θ XRD patterns (figure 2). The lack of diffraction is unexpected because the RHEED patterns from the film surface after deposition (figure 2, insets) appear to show that the films are epitaxial and single crystalline, although significant modulation of the diffraction streaks indicates a high degree of surface roughness. The film deposited at condition A produced a diffraction pattern with a sharp reflection at $2\theta \sim 43.08°$, which is very close to the expected position for bulk Fe_3O_4(004), $2\theta = 43.07°$. However, the sharpness and high intensity of this peak suggest that it may instead be an MgO substrate reflection; the MgO substrates in this study typically exhibit multiple peaks due to mosaic structure and crystalline defects. The

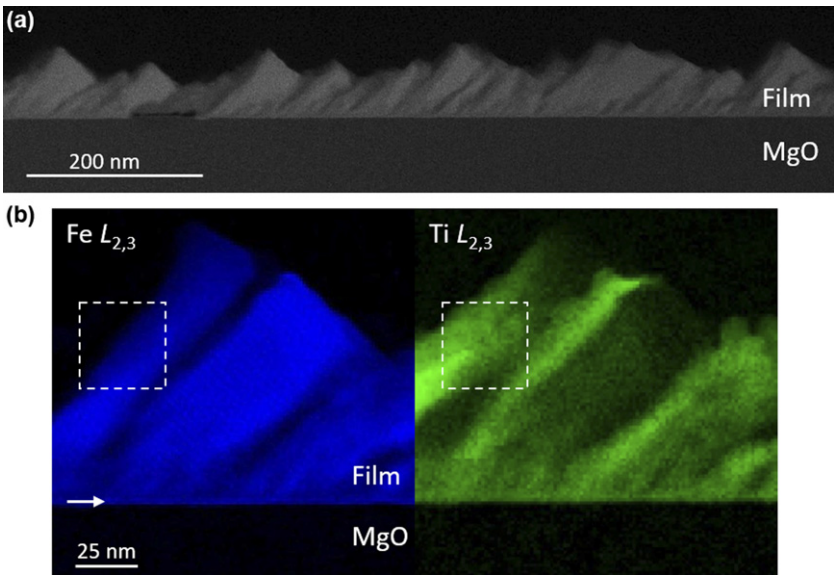

Figure 3. (a) Representative cross-sectional STEM-HAADF overview image of Fe_2TiO_4 film deposited under condition A. (b) Colorized Fe $L_{2,3}$ (left) and Ti $L_{2,3}$ (right) STEM-EELS maps. Thin layer enriched in Fe at the MgO interface is indicated by an arrow. Images taken along MgO [110] zone-axis.

Fe_2TiO_4 film deposited at condition C shows no diffraction reflections that cannot be attributed to the MgO substrate. However, very weak finite-thickness interference fringes are visible (indicated by arrows in figure 2), confirming that the diffraction peak from the film occurs near the MgO(002) substrate reflection and is thus obscured. The diffraction pattern for the Fe_2TiO_4 film deposited at condition C after annealing in vacuum presents some diffraction intensity near the expected position ($2\theta = 42.349°$) for the Fe_2TiO_4(004) reflection, indicating that some Ti has incorporated into the spinel lattice during the anneal. However, the incorporation has not been sufficient to fully transform the film to well-crystallized Fe_2TiO_4.

The RHEED patterns for the films deposited under the highly reducing environments of conditions D (figure 2) and E indicate that both films are fully polycrystalline, with no evidence of epitaxy. Likewise, the XRD pattern of the film deposited at condition D (figure 2) reveals no diffraction intensity near the MgO(002) reflection, confirming the lack of oriented $Fe_{2+x}Ti_xO_4$. However, a weak peak is observed near 65° 2θ, corresponding to the (200) reflection of bcc Fe. The presence of metallic Fe in this film is consistent with the XPS results in figure 1(a).

To understand the nanoscale film structure that gives rise to the somewhat unexpected cation valence trends and contradictory diffraction data for the films grown at conditions A, B, and C, we turn to STEM imaging and associated EDS maps. Figure 3(a) shows a cross-sectional STEM-HAADF image of the (nominally) Fe_2TiO_4 film deposited under condition A. The film morphology is distinctly non-uniform, and consists of 'peaks' ranging from ∼50–85 nm high, separated by lower regions ('valleys') ∼35–45 nm high. The sidewalls of the peaks are angled approximately 45° relative to the substrate surface, approximately parallel to the [111] lattice direction. The contrast observed in the film is due to compositional inhomogeneity, as confirmed by the Fe and Ti STEM-EELS maps in figure 3(b). In these maps, a very thin, flat layer enriched in Fe is present at the MgO interface. This well-defined film gives way after only ∼2 nm to significant spatial inhomogeneity of both composition and morphology. Alternating bands of Fe-rich and Ti-rich regions run from the Fe-rich layer at the MgO interface to the surface, following the ∼45° angles of the surface peaks. Within this inhomogeneous region, it appears that only a small fraction of Ti remains in the Fe-rich regions, and close inspection of the Ti-rich regions reveals little or no Fe signal. A certain directionality can be discerned in figures 3(a) and (b), with peaks and compositional bands running from lower left to upper right of the images, parallel to the [111] lattice direction. This directionality persisted across the film surface, as observed in secondary electron images of the surface (supplementary material figure S3).

High resolution STEM-HAADF images of the Ti-rich and Fe-rich regions reveal that the crystalline structure differs in the two areas, as shown in figure 4. In the Ti-rich area, the lattice is a cubic arrangement of atoms (rotated slightly in the plane of the image) that can be mapped to the rutile polymorph of TiO_2 when viewed along the [100] direction. The observed lattice spacing in this image is measured as 0.64–0.69 nm, which correlates well with the expected spacing of 0.65 nm when viewed along the rutile [100] direction. The Fe-rich area, in contrast, exhibits a different periodic lattice structure. This atomic arrangement can be correlated with the spinel structure of Fe_3O_4 viewed along the [110] direction. In this direction, the brighter spots are densely occupied octahedral site columns and the dimmer spots are less densely occupied octahedral and tetrahedral site columns of the spinel structure [40]. From these lattice images, it is evident that the film deposited at condition A exhibits phase separation into rutile TiO_2 and spinel Fe_3O_4.

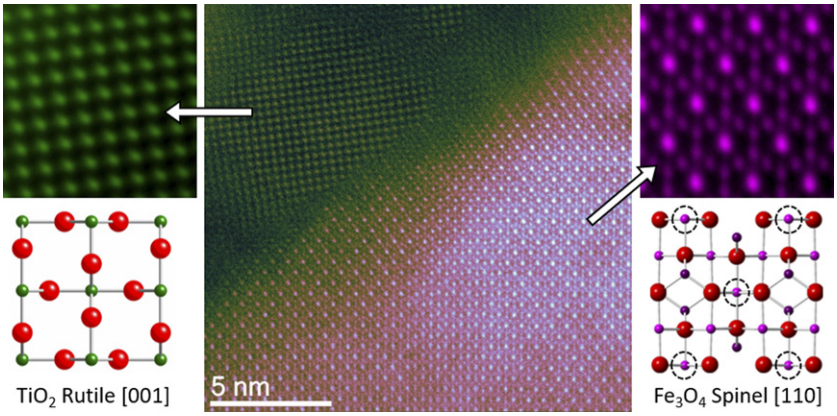

Figure 4. Colorized, drift-corrected STEM-HAADF images taken from the dashed box in figure 3, showing the Fe-rich (magenta) and Ti-rich (green) regions of the Fe_2TiO_4 film deposited under condition A. Ball-and-stick models of rutile TiO_2 in the [001] viewing direction and spinel Fe_3O_4 in the [110] viewing direction are shown for comparison to the template-matched STEM-HAADF images taken from the indicated areas. The circled octahedral Fe atom columns in the Fe_3O_4 model have a higher occupancy than the other columns, such that they appear brighter in the STEM-HAADF imaging.

The film deposited at condition C shows a markedly different structure by STEM. As shown in figure 5(a), although the Fe_2TiO_4 film still exhibits surface roughness, it is smoother and more uniform than the film deposited at condition A. The strongly faceted 'peaks' with ∼45° walls present in the film at condition A are absent in this film, and instead the surface roughness consists of a hatched distribution of rounded nanoscale clusters. High resolution imaging (figure 5(b)) confirms that the lattice is entirely the spinel structure, although the film contains disordered regions. These disordered regions correspond to Ti enrichment, as revealed by the Fe and Ti STEM-EELS maps in figure 5(c). This segregation is not as complete as for the film at condition A; although nanoscale regions show some Fe or Ti enrichment, there are no regions where one cation is nearly absent in favour of the other. As stated above, the crystal structure of the film is uniformly spinel; no evidence of rutile or other secondary phases was observed.

4. Discussion

It has long been recognized that the oxidation conditions during the synthesis of Fe_2TiO_4 must be controlled to achieve films or bulk materials that consist exclusively of Fe^{2+} [19, 23]. The results presented here demonstrate that the oxidation environment during thin film synthesis of Fe_2TiO_4 dictates not only the Fe^{2+}/Fe^{3+} content of the film, but also controls the incorporation (or, conversely, segregation) of Ti, as well as the overall film morphology. The correlations between MBE deposition conditions, Ti incorporation, and Fe valence are summarized in figure 6. In this plot, Ti incorporation is qualitatively assessed for all films by calculating the apparent Ti concentration from the XPS data; Ti content x greater than unity indicates that Ti has segregated to the film surface, which correlates with poor incorporation into the spinel lattice. The quantitative Fe^{2+} fraction from Fe K-edge XANES spectra is also plotted in figure 6 for films deposited under conditions B and C, and a qualitative assessment of Fe valence from Fe 2p XPS spectra is indicated for the other films in this study.

Under highly oxidizing conditions (condition A), Fe_2TiO_4 was not formed. Instead, the film separated into epitaxial Fe_3O_4 and rutile TiO_2. Both phases appear to be nearly pure, with almost no incorporation of Fe in TiO_2 or Ti in Fe_3O_4. The XPS spectra from this film bears this out: the Fe 2p core level lineshape is nearly identical to that for Fe_3O_4 (figure 1(a)), indicating that no Ti has incorporated and reduced neighbouring Fe^{3+} to Fe^{2+}, and the Ti 2p core level position matches that of $SrTiO_3$, exhibiting a shift of ∼0.2 eV and narrowing relative to the spectra from films deposited at other conditions (figure 1(c)).

In the TiO_2–Fe_3O_4 film deposited under condition A, phase separation is accompanied by considerable surface roughness. The Fe_3O_4 'peaks' are found by cross-sectional STEM imaging (figure 3) to possess edges that are oriented ∼45° relative to the substrate surface. We conclude from this that the edges are (111) facets of the spinel structure. The (111) surface of Fe_3O_4 is a low energy surface [3, 16, 41]. Note that in figure 3, the Fe_3O_4 faceting direction and the orientation of TiO_2 (darker contrast in figure 3(a)) relative to Fe_3O_4 (lighter contrast in figure 3(a)) appear to be directional, i.e., in figure 3(a), the Fe_3O_4 peaks are aligned such that the 45° surfaces are parallel to each other, and the TiO_2 regions appear on the left side of the peaks. This directional faceting persists across the surface, as also seen in secondary electron images in supplementary figure 3. We hypothesize that this directionality arose from the deposition geometry: the Fe and Ti effusion cells are angled at ∼51° from the substrate surface, and situated nearly opposite each other in the deposition chamber. Deposition from these angled sources, in the absence of substrate rotation, may have exaggerated the initial surface roughness as the film thickness increased. The initial surface roughness may have been enhanced by Ti segregation to the surface of the growing film, as evidenced by the thin, nearly pure Fe_3O_4 layer observed at the MgO(001) interface in STEM-EELS maps (figure 3(b)).

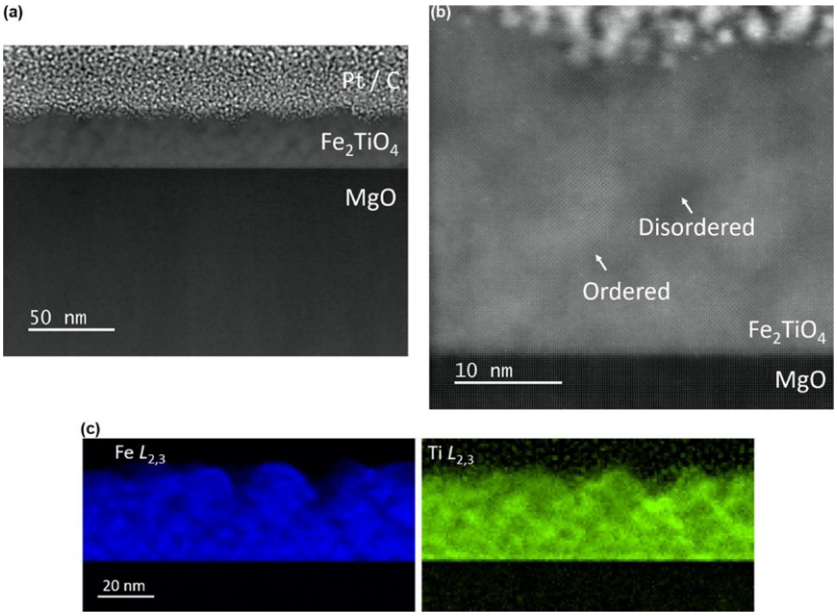

Figure 5. (a) Representative cross-sectional STEM-HAADF overview image of Fe_2TiO_4 film deposited under condition C. (b) Lattice-resolved STEM-HAADF image of spinel film structure. Crystallographically ordered and disordered regions are indicated. (c) Colorized Fe $L_{2,3}$ (left) and Ti $_{L2,3}$ (right) STEM-EELS maps. Images taken along MgO [100] zone-axis.

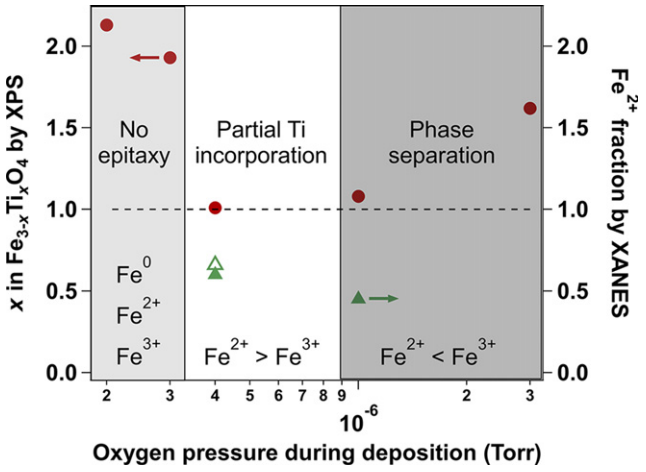

Figure 6. Summary of relationship between deposition conditions (oxygen partial pressure) and resulting film characteristics. Incorporation of Ti into the spinel lattice is anti-correlated with the apparent Ti concentration measured by surface-sensitive XPS (left axis, filled circles). The Fe^{2+} fraction (filled and open triangles; open triangle is after annealing) is taken from the edge jump position of Fe K-edge XANES spectra.

Dramatic differences are observed in the morphology of Fe_2TiO_4 films deposited under less oxidizing conditions. Deposition under much milder condition C, in which the oxygen pressure is lowered by nearly an order of magnitude, the oxygen plasma is not used, and the substrate temperature is decreased from 375 °C to 250 °C, results in a film with Ti incorporation into the Fe_3O_4 lattice without the formation of a secondary phase of TiO_2. The Fe_2TiO_4 film surface, while rough, does not exhibit faceting (note that films deposited under conditions B, C, D, and E were rotated during deposition). However, nanoscale segregation of Ti within the spinel lattice is observed in STEM-EELS maps (figure 5(c)). This segregation is correlated with a significant fraction of Fe^{3+} in the Fe 2p core level spectrum (figure 1(a)), indicating that, despite the milder oxidation conditions, the film is still over-oxidized. Annealing this film at 400 °C for 120 min in vacuum further reduces Fe^{3+} to Fe^{2+} (figures 1(a) and (b)), but little of this Fe^{2+} occupies tetrahedral sites in the spinel lattice (figure 1(c)), and the bulk crystal structure does not become that of Fe_2TiO_4 (figure 2).

Finally, the films deposited under more reducing conditions (conditions D and E) show that the oxidizing environment can be decreased too far; although the partial pressure of oxygen was only decreased slightly from condition C (figure 6), these films are not epitaxial and possess a significant fraction of unoxidized Fe^0. Interestingly, however, the oxidized Fe fraction appears to still be a mix of Fe^{2+} and Fe^{3+}.

To understand our deposition results, we propose a model of the low temperature deposition of Fe_2TiO_4 as a function of oxygen pressure and gain insight into the thermodynamics of the Fe–Ti–O system at low temperature and pressure. The Fe–Ti–O phase diagram at high temperature is a complex function of composition and oxygen activity [21, 22]. The enthalpy of formation of Fe_2TiO_4 is -1496 ± 5 kJ mol^{-1} [20], compared to -824.2 kJ mol^{-1} for Fe_2O_3, -944.0 kJ mol^{-1} for TiO_2, and -1118.4 kJ mol^{-1} for Fe_3O_4 [42]. There is a strong thermodynamic driving force for titanomagnetites to oxidize into phase-separated Fe_2O_3 and TiO_2 [43]. In addition, increased cation diffusivity has been observed for Fe_2TiO_4 at higher oxygen partial pressures when measured at high temperature (1400 °C) [44], and even at the low temperatures employed in MBE deposition, an increased oxygen partial pressure likely increases cation diffusivity on the growing film surface, favouring phase separation. Therefore, under the strongest oxidizing conditions achievable by OPA-MBE

(e.g., condition A), phase separation into rutile TiO_2 and Fe_3O_4 occurs. The enthalpy change of the reaction $3Fe_2TiO_4 + O_2 \rightarrow 2Fe_3O_4 + 3TiO_2$ is -577.8 kJ mol^{-1} at standard temperature and pressure, and the observation of phase separation during deposition under condition A indicates that a similar thermodynamic relation holds under those conditions. We hypothesize that the reaction does not proceed all the way to Fe_2O_3 because of the low partial pressure of oxygen; an additional contribution to the stabilization of Fe_3O_4 may be the epitaxial match to the MgO(001) substrate.

Reducing the oxygen pressure reduces this driving force for oxidation, allowing Ti to incorporate in the spinel lattice. However, the enthalpy of mixing in the titanomagnetite system is slightly positive [43], leading to a low-temperature miscibility gap, as reported previously for $Fe_{3-x}Ti_xO_4$ below 455 °C [6]: when equilibrated below this temperature, $Fe_{3-x}Ti_xO_4$ spinodally decomposes to Fe_3O_4 and Fe_2TiO_4. The low temperature employed in deposition condition C is not sufficient to overcome this thermodynamic mixing barrier and fully homogeneously incorporate Ti into the spinel lattice; some Ti segregation occurs. At the same time, the oxidative conditions are still sufficiently high to maintain some Fe^{3+} in the tetrahedral sites of the spinel lattice, forming a titanomaghemite-like material. Titanomagnetite transforms to titanomaghemite as Fe^{2+} cations are oxidized to Fe^{3+}; charge neutrality is maintained via the formation of cation vacancies [43]. This oxidation is likely to occur preferentially on the tetrahedral sites because Fe^{2+} is less stable in these sites [45]. The lattice parameter of titanomaghemite is smaller than that of titanomagnetite [46], likely nearing the lattice parameter of MgO at the fully oxidized titanomaghemite endmember. A shift of the Fe_2TiO_4(004) diffraction reflection to higher 2θ due to partial oxidation to titanomaghemite is a likely explanation for the overlap of the film and substrate diffraction peaks of the film deposited under condition C in figure 2. Annealing at high temperature in vacuum is shown to partially reduce the titanomaghemite-like film back to a titanomagnetite-like material.

In the synthesis of Fe_2TiO_4 powders [19] and single crystals [18, 47], high temperatures (900 °C–1200 °C) are employed to incorporate Ti into the Fe_3O_4 lattice. These temperatures are well above the solvus temperature of the $Fe_{3-x}Ti_xO_4$ system [6], and at these temperatures the entropy of formation of Fe_2TiO_4 dominates the enthalpy term, making Fe_2TiO_4 an entropy-stabilized oxide [20]. Furthermore, cation diffusivities are high enough at these temperatures [44] to equilibrate in the thermodynamically stable Fe_2TiO_4 phase in a reasonable timeframe. In these synthesis pathways, tuning the level of oxidation of the material to obtain stoichiometric $Fe_{3-x}Ti_xO_4$ is typically treated as a second step that also takes place at high temperature, but in an atmosphere of controlled (low) oxygen activity.

Likewise, thin film synthesis by PLD [23] resulted in substitutional Ti incorporation into the Fe_3O_4 lattice. Both the previous depositions by PLD [23] and the MBE depositions under condition C occurred under relatively low oxygen partial pressure and low temperature, but the outcome was very different: crystalline Fe_2TiO_4 by PLD and poorly crystallized material by MBE. This difference can be attributed to the high kinetic energy of species in the laser ablation plume generated during PLD compared to thermal evaporation during MBE; this high energy of the species arriving on the substrate surface facilitates surface diffusion that would otherwise be achieved only at higher substrate temperatures. Nonetheless, some Ti segregation to the film surface was observed in the films deposited by PLD [23, 26, 27].

Comparison of these results by MBE with previous film deposition by PLD [23] suggests a pathway to obtain stoichiometric, well-crystallized Fe_2TiO_4 by performing the deposition at high temperature and low oxygen partial pressure. This approach would require the use of a thermally stable substrate in place of MgO. Interdiffusion of Mg and Fe is well established at the Fe_3O_4/MgO interface at elevated temperature [40], and under our MBE conditions, Mg diffusion into the Fe_2TiO_4 film is observed at deposition temperatures as low as 375 °C (supplementary material figure S2). Potential candidate substrates include $MgAl_2O_4$(001) and Al_2O_3(0001). Epitaxial Fe_2TiO_4 has been demonstrated by PLD on both $MgAl_2O_4$(001) [25] and Al_2O_3(0001) [24]. However, both of these substrates have a larger lattice mismatch with Fe_2TiO_4 than does MgO(001) (lattice mismatch, δ, of 5.6% for $MgAl_2O_4$(001) and 9.8% for Al_2O_3(0001), compared to 1.3% for MgO(001)), which will lead to the introduction of defects such as misfit dislocations and antiphase boundaries that are likely to impact the magnetic and electrical transport properties of the film. Recent reports of improved structural and magnetic properties of epitaxial Fe_3O_4 films deposited on spinel $MgGa_2O_4$(001) and $CoGa_2O_4$(001) by PLD [48, 49] suggests that these substrates may be candidates for Fe_2TiO_4 deposition, although their high temperature stability has not been evaluated.

5. Conclusions

Epitaxial thin films of Fe_2TiO_4 were deposited by MBE at low temperature under various oxidation conditions. Structural characterization indicated that well-crystallized Fe_2TiO_4 was not formed under any conditions studied here. Detailed spectroscopy and microscopy revealed that, under strongly oxidizing conditions, phase separation into TiO_2 and Fe_3O_4 occurred. Ti incorporation could be achieved under less oxidizing conditions, but the concurrent presence of tetrahedral Fe^{2+} was not observed. Lowering the oxygen partial pressure even slightly further resulted in the presence of Fe^0 in the film. These results illustrate that both the spatial segregation of Ti and the Fe valence are extremely sensitive to the oxidation conditions during deposition. A pathway to achieve stoichiometric, well-ordered Fe_2TiO_4 epitaxial films by utilizing much higher substrate temperatures in conjunction with low oxygen partial pressures is suggested by this work.

Acknowledgments

TCK, SRS, BEM, MEB, LW, and SAC were supported by the US DOE, Office of Science, Office of Basic Energy

Sciences (BES), Division of Materials Sciences and Engineering under award # 10122. A portion of the work was performed at the W R Wiley Environmental Molecular Sciences Laboratory, a DOE User Facility sponsored by the Office of Biological and Environmental Research and located at Pacific Northwest National Laboratory (PNNL). STEM imaging was performed in the Radiological Microscopy Suite, located in the Radiochemical Processing Laboratory (RPL) at PNNL. PNNL is a multiprogram national laboratory operated for DOE by Battelle. RP and RBC gratefully acknowledge funding from the National Science Foundation Division of Materials Research through grant DMR-1809847. XY acknowledges funding support from MOE Tier 2 grant MOE2017-T2-2-139. The Singapore Synchrotron Light Source (SSLS) is a National Research Infrastructure under the National Research Foundation, Singapore.

Data availability statement

All data that support the findings of this study are included within the article (and any supplementary files).

ORCID iDs

Tiffany C Kaspar https://orcid.org/0000-0003-2816-7569
Steven R Spurgeon https://orcid.org/0000-0003-1218-839X
Tamara Isaacs-Smith https://orcid.org/0000-0002-1096-153X
Ryan B Comes https://orcid.org/0000-0002-5304-6921

References

[1] Weiss W and Ranke W 2002 *Prog. Surf. Sci.* **70** 1–151
[2] Tartaj P, Morales M P, Gonzalez-Carreño T, Veintemillas-Verdaguer S and Serna C J 2011 *Adv. Mater.* **23** 5243–9
[3] Santos-Carballal D, Roldan A, Grau-Crespo R and de Leeuw N H 2014 *Phys. Chem. Chem. Phys.* **16** 21082–97
[4] Taffa D H, Dillert R, Ulpe A C, Bauerfeind K C L, Bredow T, Bahnemann D W and Wark M 2017 *J. Photon. Energy* **7** 012009
[5] Sutka A and Gross K A 2016 *Sens. Actuators* B **222** 95–105
[6] Price G D 1981 *Geophys. J. Int.* **66** 751–5
[7] Wechsler B A, Lindsley D H and Prewitt C T 1984 *Am. Mineral.* **69** 754–70
[8] Brabers V A M 1995 *Physica* B **205** 143–52
[9] Bertinetti S, Hanna K, Minella M, Minero C and Vione D 2019 *Desalin. Water Treat.* **151** 117–27
[10] Marsac R, Pasturel M and Hanna K 2017 *J. Phys. Chem* C **121** 11399–406
[11] Yang S, He H, Wu D, Chen D, Ma Y, Li X, Zhu J and Yuan P 2009 *Ind. Eng. Chem. Res.* **48** 9915–21
[12] Zhong Y, Liang X, Zhong Y, Zhu J, Zhu S, Yuan P, He H and Zhang J 2012 *Water Res.* **46** 4633–44
[13] Katayama T, Kurauchi Y, Mo S, Gu K, Chikamatsu A, Galiullina L and Hasegawa T 2019 *Cryst. Growth Des.* **19** 902–6
[14] Seki M, Tabata H, Ohta H, Inaba K and Kobayashi S 2011 *Appl. Phys. Lett.* **99** 242504
[15] Fleet M E 1981 *Acta Crystallogr.* B **37** 917–20
[16] Parkinson G S 2016 *Surf. Sci. Rep.* **71** 272–365
[17] Walz F 2002 *J. Phys.: Condens. Matter* **14** R285–340
[18] Bosi F, Halenius U and Skogby H 2009 *Am. Mineral.* **94** 181–9
[19] Pearce C I, Henderson C M B, Telling N D, Pattrick R A D, Charnock J M, Coker V S, Arenholz E, Tuna F and van der Laan G 2010 *Am. Mineral.* **95** 425–39
[20] Lilova K I, Pearce C I, Gorski C, Rosso K M and Navrotsky A 2012 *Am. Mineral.* **97** 1330–8
[21] Itoh S 1999 *ISIJ Int.* **39** 1107–15
[22] Taylor R W 1964 *Nature* **203** 1016
[23] Droubay T C, Pearce C I, Ilton E S, Engelhard M H, Jiang W, Heald S M, Arenholz E, Shutthanandan V and Rosso K M 2011 *Phys. Rev.* B **84** 125443
[24] Murase H, Fujita K, Murai S and Tanaka K 2009 *Mater. Trans.* **50** 1076–80
[25] Yamahara H, Seki M, Adachi M, Takahashi M, Nasu H, Horiba K, Kumigashira H and Tabata H 2015 *J. Appl. Phys.* **118** 063905
[26] Stoerzinger K A, Pearce C I, Droubay T C, Shutthanandan V, Liu Z, Arenholz E and Rosso K M 2019 *Langmuir* **35** 13872–9
[27] Stoerzinger K A, Pearce C I, Droubay T C, Shutthanandan V, Shavorskiy A, Bluhm H and Rosso K M 2017 *J. Phys. Chem* C **121** 19288–95
[28] Gao Y, Kim Y J and Chambers S A 1998 *J. Mater. Res.* **13** 2003–14
[29] Gao Y, Kim Y J, Chambers S A and Bai G 1997 *J. Vac. Sci. Technol.* A **15** 332–9
[30] Kim Y J, Gao Y and Chambers S A 1997 *Surf. Sci.* **371** 358–70
[31] Chambers S A, Droubay T C, Kaspar T C, Nayyar I H, McBriarty M E, Heald S M, Keavney D J, Bowden M E and Sushko P V 2017 *Adv. Funct. Mater.* **27** 1605040
[32] Scafetta M D, Kaspar T C, Bowden M E, Spurgeon S R, Matthews B and Chambers S A 2020 *ACS Omega* **5** 3240–9
[33] Scafetta M D, Yang Z, Spurgeon S R, Bowden M E, Kaspar T C, Heald S M and Chambers S A 2019 *J. Vac. Sci. Technol.* A **37** 031511
[34] Kaspar T C, Bowden M E, Wang C, Shutthanandan V, Manandhar S, van Ginhoven R M, Wirth B D and Kurtz R J 2014 *Thin Solid Films* **550** 1–9
[35] Jones L, Yang H, Pennycook T J, Marshall M S J, Van Aert S, Browning N D, Castell M R and Nellist P D 2015 *Adv. Struct. Chem. Imaging* **1** 8
[36] Droubay T and Chambers S A 2001 *Phys. Rev.* B **64** 205414
[37] Biesinger M C, Payne B P, Grosvenor A P, Lau L W M, Gerson A R and Smart R S C 2011 *Appl. Surf. Sci.* **257** 2717–30
[38] Grosvenor A P, Kobe B A, Biesinger M C and McIntyre N S 2004 *Surf. Interface Anal.* **36** 1564–74
[39] Yeh J J and Lindau I 1985 *At. Data Nucl. Data Tables* **32** 1–155
[40] Wangoh L W, Yang Z, Wang L, Bowden M E, Yin X, Wee A T S, Mueller K T, Murugesan V and Du Y 2020 *ACS Nano* **14** 14887–94
[41] Mishra R K and Thomas G 1977 *J. Appl. Phys.* **48** 4576–80
[42] Lide D R 2003 *CRC Handbook of Chemistry and Physics* (Boca Raton, FL: CRC Press)
[43] Lilova K I, Pearce C I, Rosso K M and Navrotsky A 2014 *Chemphyschem* **15** 3655–62
[44] Freer R and Hauptman Z 1978 *Phys. Earth Planet. Inter.* **16** 223–31
[45] Sickafus K E, Wills J M and Grimes N W 1999 *J. Am. Ceram. Soc.* **82** 3279–92
[46] Zhou W, Peacor D R, Van der Voo R and Mansfield J F 1999 *J. Geophys. Res.* **104** 17689–702
[47] Brabers V A M, Whall T E and Knapen P S A 1984 *J. Cryst. Growth* **69** 101–7
[48] Singh A V, Srivastava A, Mohammadi J B, Regmi S, Bhat U, Datta R, Mewes T and Gupta A 2019 *J. Appl. Phys.* **126** 093902
[49] Srivastava A, Singh A V, Mohammadi J B, Mewes C, Gupta A and Mewes T 2020 *IEEE Trans. Magn.* **56** 6100506